Revista Mexicana de Astronomía y Astrofísica, 61, 84-97, (2025)

OPEN ACCESS https://doi.org/10.22201/ia.01851101p.2025.61.02.08

Lithium in V505 Per

Gloria Koenigsberger[1], Werner Schmutz[2], Catherine Pilachowski[3], Alan R. Mejía-Nava[4], Derek Sikorski[5] and María Cordero[3]

[1]*Instituto de Ciencias Físicas, Universidad Nacional Autónoma de México, Ave. Universidad S/N, Cuernavaca, Morelos, 62210, México.*
[2]*Physikalisch-Meteorologisches Observatorium Davos and World Radiation Center, Dorfstrasse 33, CH-7260 Davos Dorf, Switzerland.*
[3]*Department of Astronomy, Indiana University, Bloomington, Indiana, USA.*
[4]*Universidad Autónoma del Estado de Morelos, Cuernavaca, Morelos, México.*
[5]*Institute for Astronomy, University of Hawai'i, 2680 Woodlawn Drive, Honolulu, HI 96822, USA.*

Keywords: *Stars: binaries:eclipsing, Stars: binaries: spectroscopic, Stars: chemical abundances*

Abstract

We determined the surface lithium abundance of the eclipsing binary components in V 505 Per (HIP 10961) to be $A(Li)$=2.65±0.07 and 2.35±0.1, which supports the rather unexpected conclusion that their surface Li abundances differ. We find effective temperatures of 6600 K + 6550 K (∼150 K higher than previously reported), which places the stars at the hot limit of the Lithium Dip, thus alleviating the previously suggested discrepancy with cluster stars of similar ages and temperatures. These temperatures are also more consistent with the system's *Gaia* spectral energy distribution. Our iron abundances, $[Fe/H] = -0.15 \pm 0.07$ and -0.25 ± 0.1, agree with the predictions of the higher temperatures deduced from our spectra and from the evolutionary tracks. The rotation rate implied by our line profiles, 12.5±1 km s^{-1}, is smaller than the synchronous rotation rate, which is a curious result given the circular orbit and the age of the system.

Resumen

El análisis de un espectro de alta dispersión del sistema binario eclipsante V505 Per (=HIP 10961) resulta en abundancias de litio de $A(Li)$=2.65±0.07 y 2.35±0.1 por componente, consistentes con los encontrados en un estudio anterior, pero con temperaturas efectivas ∼150 grados mayores que en estudios previos, 6600 K + 6550 K. Las nuevas temperaturas colocan a las estrellas en el límite caliente del "Lithium Dip", eliminando la inconsistencia con resultados de estrellas en cúmulos de la misma edad y masa. Estas temperaturas son consistentes con la distribución espectral de energía de Gaia. Las abundancias de hierro, $[Fe/H] = -0.15 \pm 0.07$ y -0.25 ± 0.1, concuerdan con las predicciones de temperaturas más altas deducidas de nuestros espectros y de las trayectorias evolutivas. La velocidad de rotación es 12.5 ± 1 km s^{-1}, un valor menor al valor de rotación síncrona, situación curiosa dada la órbita circular y la edad del sistema binario.

Corresponding author: G. Koenigsberger *E-mail address:* gloria@icf.unam.mx
Received: November 3, 2025 **Accepted:** May 27, 2025

1. Introduction

Double-line eclipsing binaries are among the most important astrophysical objects available for understanding various physical processes. One of the many astrophysical problems they can be used to address is the one associated with the manner in which nuclear processed material is transported from inner layers to the stellar surface. This is because the two stars in the system can be assumed to have formed from the same molecular cloud at the same time, and thus have the same age. If they have the same mass, they are expected to follow identical evolutionary paths as their interior mixing processes should be the same. Any difference in chemical surface abundance would serve to quantify the differences in the mixing processes.

V505 Persei (HD 14384, HIP 10961) is a short-period, double-line eclipsing binary system in which both stars are spectroscopically very similar. The slightly brighter, larger, and more massive of the two is referred to as component A, and its companion is referred to as component B. The orbital period is well-known to be 4.22 d although, as noted by Southworth (2021), it was first thought to be 2.11 d, half the actual value, due to the nearly identical shape of the two eclipses.[1] The two components have nearly the same mass: 1.27 $M_\odot$+1.25 $M_\odot$) and radii (1.29 $R_\odot$+1.26 $R_\odot$ (Southworth, 2021, henceforth S21).The effective temperatures T_{eff}, determined by Tomasella et al. (2008) (henceforth T08), are also very similar (6515±50 K and 6460±50 K, respectively).

Although most of its properties appear to be determined with exquisite precision, there is a significant spread in the published metallicity values. T08 obtained

[1]Note that automatic period-search algorithms also commit the same mistake even in recent times (Prša et al., 2022)

[M/H]=−0.12±0.03 from a χ^2 model fit to the observed spectra. Also using model fits to spectral observations Baugh et al. (2013) obtained a similar result, $[Fe/H]$ =-0.15±0.03. According to T08, this metallicity is consistent with V505 Per's ∼1 Gyr age and the idea that element diffusion during this time reduced the surface metallicity from an initial ∼solar value. Casagrande et al. (2011a) found $[M/H]$=−0.25 based on a re-assessment of the photometric measurements listed in the Holmberg et al. (2007) Geneva-Copenhagen survey of the Solar neighborhood, where it was listed with $[M/H]$=−0.35. In contrast to these sub-solar values, S21 found a slightly super-solar metal abundance by comparing the observed properties with theoretical mass-radius and mass-effective temperature diagrams.[2] Hence, as suggested by S21, a reappraisal of metallicity is warranted.

Another curious aspect is the conclusion reached by Baugh et al. (2013) regarding the lithium abundance in these two stars. They found star A to have A(Li)∼2.67±0.1 and star B to have A(Li)∼ 2.42 ± 0.2. The T08 temperatures place both stars within the *Lithium Dip*, a region in the $A(Li)$ *vs.* T_{eff} diagram within the temperature range ∼6300 K- 6600 K, in which the surface lithium abundance is severely depleted compared to stars that are hotter and cooler than this temperature range (Boesgaard & Tripicco, 1986; Thorburn et al., 1993; do Nascimento et al., 2000). The Baugh et al. (2013) lithium abundance values are 2-5 times larger than the detections and upper limits derived in the similar metallicity and intermediate-age open clusters NGC 752 and 3680, as well as the more metal-rich and younger Hyades and Praesepe. Baugh et al. (2013) suggested that the higher A(Li) values supported the hypothesis that different rotational evolution of stars in short-period binaries affect their lithium depletion, making them different from single stars. For massive stars, Pavlovski et al. (2023) have concluded that the interior chemical element transport is not as efficient in binary star components as in their single-star counterparts in the same mass regime, and evolutionary stage. Thus, the question of internal mixing is relevant across the Hertzprung-Russell diagram.

In this paper we analyze a high resolution echelle spectrum obtained at orbital phase 0.97, when the lines of both stars are well resolved, in order to further constrain the metallicity, projected rotation velocity and lithium abundance in both components. In § 2, we describe the observations and data reduction. In § 3, we perform a light curve analysis of the *TESS* data. In § 4, we analyze the $[Fe/H]$ abundances by both a curve of growth method and a detailed comparison of the theoretical spectral lines to the observed line profiles. In § 5, we constrain the lithium abundance, and in §6, we discuss the results, and in § 7, we summarize the conclusions.

[2]These results implied a fractional metal abundance Z=0.017 and an age 1.050±0.050 Gyr. S21 noted that the $[M/H] \sim -0.12$ value could be excluded from his results because it corresponds to Z=0.0116 (for a heavy-element mixture such that the solar metallicity is $Z_\odot$=0.01524), a value outside the bounds of the range allowed by the theoretical models.

2. Observations

V505 Per (=TIC 348517784) was observed by the TESS satellite (Ricker et al., 2015) in sectors 18 (2019), 58 (2022), and 85 (2024). The 2-minute cadence data files were downloaded from the Mikulski Archive for Space Telescopes (Swade et al., 2019) using search_lightcurve (Ginsburg et al., 2019). These files contain the Simple Aperture Photometry fluxes (SAP flux) and the background counts as reduced by the TESS pipeline. The light curves are the result of aperture photometry, which gives the total counts measured from the TESS images within the photometric aperture. The light curves were extracted and normalized using the Lightkurve Collaboration software (Lightkurve Collaboration et al., 2018), excluding data that do not have a quality equal to zero and epochs with background counts higher than 50000 e^-/s, where typical count rates of the targets were 400,000 e^-/s. We also excluded the first part of the Sector 18 light curve earlier than BTJD 1794 d because the fluxes rose to 1.01 of the normalized uneclipsed level. It is not clear whether this is a real flux change or something else, and there is no other similar deviation from regular repeating orbital variations in the light curve.

Our spectroscopic observations of V505 Per were obtained on 2011 Sept 16 and 20 at the Kitt Peak National Observatory Coudé Feed telescope using the echelle grating with a slit width of 250 μm, Camera 5, and the F3KB CCD. The echelle grating provides a reciprocal dispersion of 1.9 Å/mm at λ6697 Å which, with the CCD 0.015 mm/pixel, provides a resolution R= 110000 at this wavelength.[3] Flat fields and biases were obtained throughout the night of September 20 and at the beginning and end of the night of September 16. The Julian Dates (-2400000) of our observations are 2455821.8953 and 2455825.9871, which correspond to orbital phases 0.9772 and 0.9464, respectively, based on an initial epoch T_0=JD 2458798.516720 and orbital period P=4.2220216 d given by S21 (but see below). The orbital phases are defined such that φ=0 corresponds to the deeper of the two eclipses, which occurs when star A is eclipsed by its companion B.

The Sept 16 spectrum was obtained just before ingress of primary eclipse (first contact occurs at φ ∼0.985 see Figure 2 of S21). At this phase, the lines of the two stars are barely resolved, with their centroids separated by only 19 km s^{-1}. The September 20 spectrum was obtained sufficiently far from conjunction for the lines of the two stellar components to be well separated (58 km s^{-1}), allowing a more straightforward analysis by avoiding the blending effects.

The echelle spectra were reduced according to standard methods available in IRAF. Since the wavelength calibration is not absolute, we opted to shift the spectrum so that the absorption lines belonging to the star approaching the observer are centered on the laboratory wavelengths.

[3]Willmarth, Daryl, 2.1m Coudé Spectrograph Instrument Manual, NOAO, Jan. 5, 1996.

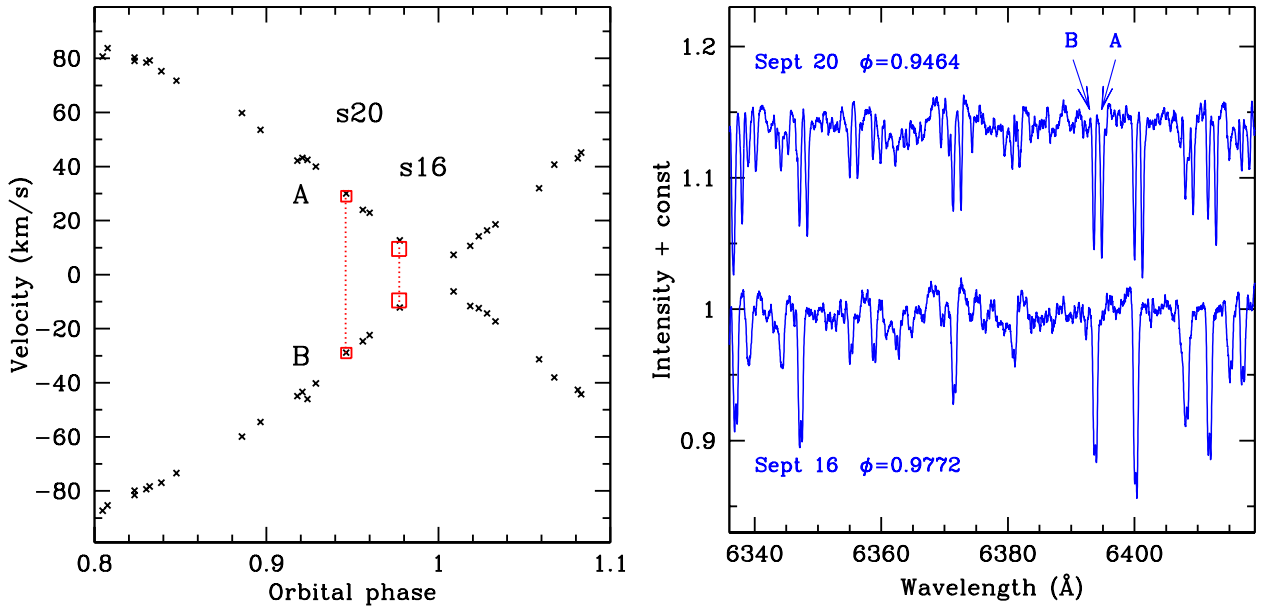

Figure 1. Left: Radial velocity curves near the ϕ=0.00 eclipse, constructed from the data in SB9 catalogue (crosses). The dotted vertical lines indicate the RV separation (ΔRV) of components A and B in our two spectra, which were obtained on September 16 and 20. At phase 0, star B is in front of star A. **Right:** Spectra of V505 Per obtained at φ=0.9464 (20 September, top) and φ=0.9778 (September 16 bottom), phases computed using Eq. 1. A constant vertical shift was introduced in the spectrum of September 20 for clarity. The star B wavelength scale is centered on the laboratory wavelength, so star A's spectrum is shifted by +58 km s^{-1} with respect to that of star B on Sept. 20 (as indicated by labels A and B). The two components were not resolved on September 16.

In our spectra, this is the lower-mass component (star B), so this is the spectrum that is centered on the laboratory wavelengths. The primary lines appear to be shifted by +58 km s^{-1}.

A compendium of V505 Per radial velocities is available in The Ninth Catalogue of Spectroscopic Binary Orbits (Pourbaix et al., 2004)[4], from which we plot in Figure 1 shows the data for the orbital phase interval 0.8 – 1.1. The location corresponding to the two observations is indicated. Since we only have relative RV measurements, we connect the data points for the primary and the secondary with a dotted line and shift them vertically on this plot to show that the relative RVs are fully consistent with published radial velocity curves.

The standard method to correct for the echelle blaze was applied in order to normalize each of the spectral orders. Corrections for a high-frequency intensity oscillation along the normalized orders were manually corrected by fitting a high-order polynomial to the visually fitted continuum level. This resulted in spectral orders where the continuum generally lies at an intensity level of unity $\pm 1\% - 2\%$. A sample spectrum is shown in Figure 1. The echelle spectra have S/N$\sim$100 per 0.02 Å pixel. For the analysis, we applied a boxcar 5-point smoothing to enhance the S/N.

[4]http://sb9.astro.ulb.ac.be

3. Light curve analysis

The TESS light curves comprise 15 primary and 14 secondary minima. The primary minima have a depth of $\sim$61.8 % of the out of eclipse light level, and the 14 secondary minima have a depth of $\sim$62.8 %. The individual light curves show a scatter in the depths of $\sim$0.1 %.

The epochs of the light curve minima were measured using the method proposed by Kwee & van Woerden (1956). The average estimated uncertainty of the method is 0.8 sec, and standard deviation of the observed minima from a fitted straight line to the epochs of minima timing is 1.1 sec.

The fits to both primary and secondary minima yield the same period within the uncertainties, from which the following ephemeris was derived:

$$\begin{aligned} \mathrm{BJD\,(Min\,I)} = \quad & 2458798.51672(\pm 3\,10^{-5}) + \\ & 4.22201933(\pm 2\,10^{-8}) \times E \end{aligned} \qquad (1)$$

where E is an integer number corresponding to the orbital cycle. The zero epoch agrees with the time determined by S21, but the uncertainty of our determination is a factor six larger. The period of our determination is a factor of hundred more precise than that given by S21 because of the larger time base available to us.

We analyzed the folded light curve from all three TESS sectors. In a partially eclipsing systems, only the sum of the stellar radii of the two stars can be derived from the light curve, but not their ratio. Hence, we first explored

Table 1. Parameters from *TESS* light curve fit and literature

Parameter	Value	Notes
q	0.9868 (fixed)	RV curve S21
$a\sin(i)$ ($R_\odot$)	14.974 (fixed)	RV curve S21
i deg	87.859 (fitted)	light curve
a ($R_\odot$)	14.984	derived from above
$(R_A+R_B)/a$	0.1714 (fitted)	light curve
R_A+R_B ($R_\odot$)	2.5685	derived from above
T_B/T_A	0.9928 (fitted)	light curve
R_B/R_A	0.97895 (free)	Ev. Tracks

the possible range of radii ratios that could reproduce the observed light curve and found that radii ratios $rr = R_B/R_A$ in the range 0.85–1.0 yield identical light curves, all of which fit the observed one. Such a broad range of rr values introduces a large uncertainty. Thus, to further constrain the possible values, we analyzed the properties of the evolutionary tracks.

We obtained the evolutionary tracks for 1.2745 $M_\odot$ (star A) and 1.2577 $M_\odot$ (star B) by interpolating the models given by Mowlavi et al. (2012) for solar metallicity (Z=0.014) and metallicity corresponding to $[Fe/H]$ =-0.146 (Z=0.010). We extracted from these models the radii and T_{eff} as a function of age, from which we then calculated R_B/R_A, R_A+R_B and T_{eff} also as functions of age. The results are shown in Figure 2.

From the light curve solutions we get the value of the sum of the stellar radii in units of the projected orbital separation, r_A+r_B, where $r_i = R_i/a$, with a the semi-major axis of the orbit, which is obtained from the solution of the radial velocity curve (a=14.984 $R_\odot$, S21's Table V). Our light curve solution yields $(R_A+R_B)/a$=0.1714. With the above value of a, this yields R_A+R_B = 2.5685±0.001, where the uncertainty corresponds to the different results obtained from fitting the mean of all *TESS* sectors.[5] The top panel of Figure 2 shows that R_A+R_B = 2.5685 corresponds to an age 1.295 Gyr if the stars have Z=0.010 and 1.571 Gyr if they have an approximate solar metallicity. Inspection of the second and third panels in this figure shows that the predicted temperature ratio and radius ratio do not have a very strong dependence on the metallicity. For both metallicities T_{Beff}/T_{Aeff} =0.9927, similar to the 0.9328 value obtained from the light curve fit, and rr=0.97895±0.00005.

Whereas the temperature ratio is not very sensitive to metallicity, the actual temperature has a very strong dependence on metallicity. The bottom panel of Figure 2 illustrates star A's effective temperature as a function of age for the two analyzed metallicities. For an approximately

[5]Results for the individual sectors are as follows: (T_B/T_A, R_A+R_B, i, M_A+M_B)=(0.99270, 2.5691, 87.869deg, 2.53) for Sector 18; =(0.99272, 2.5684, 87.851, 2.53) for Sector 58; =(0.99280, 2.5694, 87.851, 2.53) for Sector 85. All fits performed with PHOEBE used rr=0.979

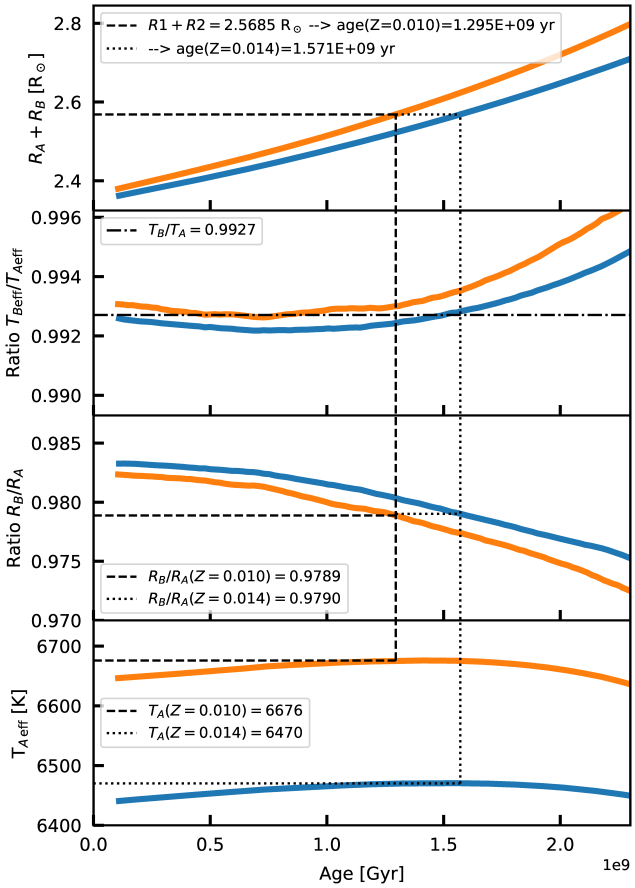

Figure 2. Evolutionary tracks for a stellar pair of M_1 = 1.2747 + M_2 = 1.2579 $M_\odot$ with solar metallicity (Z=0.014, blue) and for Z=0.010 (orange). The absicssa gives the time after the star has reached the ZAMS. The ordinate is as follows from the top to the bottom panel: the sum of the two stars' radii, R_A+R_B; the effective temperature ratio, T_{Beff}/T_{Aeff}; radii-ratio, R_B/R_A; and the value of T_{Aeff}. The R_A+R_B value is obtained directly from the solutions to the light curve and radial velocity curve, and its value for V505 Per then determines the age which, in turn, constrains the remaining parameters. The dash line gives their value for Z=0.010 and the dotted line for Z=0.014 (close to solar, $[Fe/H = -0.037)$.

solar metallicity, the temperatures are within the range determined by T08 (with the S21 uncertainties). However, the system is significantly older (1.57 Gyr instead of ~1 Gyr). However, if instead the $[Fe/H]$ values are as low as determined by Baugh et al. (2013) and Casagrande et al. (2011b), then T_{eff} must be higher than determined by T08. The bottom panel of Figure 2 indicates that T_{Aeff} ~6676 K, which from the temperature ratio means that T_{Beff} ~6627 K.

4. Iron abundance

The chemical abundance analysis of a binary system requires knowledge of the effective temperature (T_{eff}), logarithm of the surface gravity (log(g)), each star's

Table 2. Fundamental parameters of V505 Per

Parameter	Literature	This paper	
P_{orb} (d)	4.2220216(.0000023)	4.22201933(10^{-8})	⋯
M_A ($M^N_\odot$)	1.2745(.0036)[a]	⋯	⋯
M_B ($M^N_\odot$)	1.2577(.0030)[a]	⋯	⋯
rr	0.9788(.0019)[b]	0.9789	0.9790
light ratio	0.9367(.0037)[c]	⋯	⋯
i	87.9166(.0030)[c]	87.859	⋯
R_A ($R^N_\odot$)	1.2941(.0016)[d]	1.2982	⋯
R_B ($R^N_\odot$)	1.2637(.0017)[d]	1.2702	⋯
$\log(g)_A(\log[cgs])$	4.3194(.0010)[e]	⋯	⋯
$\log(g)_B(\log[cgs])$	4.3343(.0010)[e]	⋯	⋯
$[Fe/H]_A$	-0.25[f1]	Tab. 3	Tab. 3
	-0.12(.03)[f2]	⋯	⋯
	-0.15(.05)[f3]	⋯	⋯
$[Fe/H]_B$	-0.12(.03)[f4]	Tab. 3	Tab. 3
z	0.017[f5]	0.014	0.010
T_{Aeff}(K)	6512(50)[g]	6470	6676
T_{Bff}(K)	6460(50)[g]	6423	6627
$V\sin(i)_A$ (km s^{-1})	15.3(1.0)[h]	12.5 (1)	12.5(1)
$V\sin(i)_B$ (km s^{-1})	15.4(1.0)[h]	12.5 (1)	12.5(1)
ξ_{th} (km s^{-1})	1.7[j]	⋯	⋯
$log(L_A/L^N_\odot)$	0.434(.0013)[k]	0.425	0.479
$log(L_B/L^N_\odot)$	0.399(.0013)[k]	0.393	0.448
Age (Gyr)	1.050(0.050)[f5]	1.571	1.295
$D(pc)$	61.19 (.62)[m]	⋯	⋯
$D(pc)$	62.03 (.10)[n]	⋯	⋯

[aa] $M^N_\odot$, $R^N_\odot$, $L^N_\odot$ are the nominal solar units given by IAU 2015 Resolution B3 (Prša et al., 2016).

[a] Masses from the radial velocity curves solution and orbital inclination=87.916 deg.

[b] Radii ratio from the light curve fit.

[c] Light ratio from the light curve fit.

[d] Stellar radii from the light curve and radial velocity solutions. T08 values are the same within their uncertainties.

[e] The S21 et al. values derive from the masses and radii. The T08 values were obtained from the spectral fits. T08 values are the same within their uncertainties.

[f1] Casagrande et al. (2011a).

[f2] T08 from their spectrum at orbital phase 0.497, when star A nearly totally eclipses its companion.

[f4] T08.

[f5] S21 isochrone fitting; z=0.017 corresponds to $[Fe/H] = +0.05$, using $z = 0.01524 \times 10^{[Fe/H]}$, assuming a solar-proportional mix, see del Burgo & Allende Prieto (2018).

[g] Effective temperatures from T08 based on Kurucz model spectra fits to the data, with uncertainty values as given by S21.

[h1] Projected equatorial rotation velocity from T08 for star A based on their spectrum at orbital phase 0.497.

[h2] Projected equatorial rotation velocity from T08 for star B based on an iterative orbital solution for which the difference in the temperature between the primary and the secondary stars and fraction of the combined system light due to the two components was calculated.

[j] Microturbulent speed as derived by Baugh et al. (2013).

[k] Luminosity from the deduced T_{eff} and radius values. S21 notes that the distance implied by these luminosities "is slightly shorter than that obtained from the Gaia EDR3 parallax, a discrepancy most easily explained by uncertainty in the 2MASS K-band apparent magnitude."

[m] S21.

[n] *Gaia* (re-interpreted) EDR3 parallaxes, Bailer-Jones et al. (2021).

contribution to the continuum spectral energy distribution (w_A and w_B), and the microturbulent velocity (ξ_{th}). The two methods used to determine chemical abundances rely heavily on theoretical stellar atmosphere models. The first is the curve of growth method. It uses the equivalent widths of numerous absorption lines measured on the observed spectrum, which are compared to those of a grid of stellar atmosphere models. The second is a direct comparison of the observed absorption line spectrum with synthetic spectra predicted by a grid of theoretical stellar atmosphere models. Both methods require precise values of the relative continuum contributions from stars A and B, w_A and w_B.

Each star's contribution to the normalized continuum is obtained from the T_{eff} and rr values as follows. Defining a weight w_i=$L_i/(L_A + L_B)$, with L_i the luminosity of each star (i=A, B), and assuming that the black-body function is a valid approximation for the visual portion of the spectral energy distribution, we can write w_A/w_B=$(R_A/R_B)^2(T_A/T_B)^4$, with $w_A + w_B$=1.

The results shown in Figure 2 indicate that both rr and T_A/T_B are insensitive to metallicity. Using their values as listed in Table 1, we find w_A/w_B=1.0740, from where w_A=0.518 and w_B=0.482. These values were used for the subsequent analyses.

4.1. Equivalent widths of Fe lines

We measured the equivalent widths (W_λ) for 26 Fe I lines in the wavelength range $\lambda\lambda$6042-6718 in the September 20 spectrum. For comparison, we chose stellar atmosphere models having the T08 and S21 effective temperature, surface gravity and relative luminosities, and the microturbulent speed from Baugh et al. (2013) (see Table 2). The Fe I abundance was determined with the *abfind* driver in the LTE spectral synthesis and line analysis code *MOOG* (Sneden et al., 2012).[6] *MOOG* uses a carefully curated list of lines of well-determined gf values to synthesize a spectrum from stellar atmosphere models. The equivalent-width method for Fe-abundance determinations has the advantage that it does not depend on rotation velocity.

We tested models with [M/H] at −0.1, −0.2, −0.3, and −0.4 dex. This resulted in abundances 7.286, 7.285, 7.284, and 7.282, respectively, for star A, and 7.212, 7.212. 7.211, and 7.209 for star B. Thus, for each star we get an average ±s.d. of $\log(Fe)_A$=7.284±0.002 and $\log(Fe)_B$=7.211±0.001.

We also ran *MOOG* with the solar equivalent widths for the same list of lines, and a solar model at 5780 K and log g = 4.4 which was computed with the same program interpolating in the MARCS model grid. Many of the lines are rather strong in the Sun and give a lower abundance than the weaker lines. We eliminated lines stronger than Log W_λ = −4.8 (∼100 mA), and got an abundance of $\log(Fe)_\odot$ = 7.43 from this set, using a microturbulence of 1 km s^{-1} (which is the accepted value for the center-of-disk, consistent with the McMath atlas (Wallace et al., 1998)).

With the definition $[Fe/H] = \log(Fe/H) - \log(Fe/H)_\odot$ and assuming the same hydrogen abundances $\log(H) = \log(H)_\odot$, the above values of $\log(Fe)$ correspond to $[Fe/H]$ =-0.146 for star A and $[Fe/H]$ =-0.219 for star B. We adopt an uncertainty of ±0.07 dex due primarily to the uncertainty in continuum placement.

The iron abundance of star A is in excellent agreement with that of Baugh et al. (2013) (−0.15±0.03) and T08 (−0.12±−0.03), both of which are based on comparisons to Kurucz (1992) model atmosphere spectra. The iron abundance that we derive for star B is marginally lower, and more in line with the −0.25 value reported by Casagrande et al. (2011b). It is even closer to the Casagrande et al. (2011b) value if a solar microturbulence of 0.8 km s^{-1}ec is assumed (which gives a flatter dependence on line strength and a solar abundance of 7.47) resulting in $[Fe/H]$ = −0.186 and −0.259 for stars A and B, respectively. Column 3 of Tab. 3 summarizes the results of this experiment.

4.2. Modeling absorption-line profiles

Synthetic spectra in the $\lambda\lambda$ 6388-6418 Å region were generated using the *Pymoogi* Python wrapper for *MOOG* (Adamow, 2017).[7] We used MARCS stellar atmospheres models (Gustafsson et al., 2008), interpolating the available grid when required to produce synthetic spectra. Each model is characterized by the effective temperature T_{eff}, the logarithm of the surface gravity $\log(g)$, and the heavy element abundance $[Fe/H]$. Our grids of models were generated for T_{eff} in the range 6450 K to 6800 K, and $[Fe/H]$ in the range −0.4 to −0.1, with fixed $\log(g)$ and ξ_{th} as listed in Column 2 of Table 2.

The single-star spectra produced by MOOG were scaled and combined to synthesize V505 Per's double-line spectrum using the scaling factors w_A=0.518, w_B=0.482, as discussed above.

A detailed comparison between synthetic and observed spectra requires rotational broadening to be applied to the synthetic-spectral lines. In order to constrain the value of v sin(i) we used the *rotBroad* function included in the *pyAstronomy* package[8] to broaden a composite synthetic spectrum to projected rotation velocities in the range 10 km s^{-1}–14 km s^{-1}. A linear limb-darkening coefficient of 0.26 was adopted from S21. Figure 3 compares the observed λ6393.6 and λ6411.6 lines to the synthetic spectra broadened to v sin(i)=12 km s^{-1} and 13 km s^{-1}. These two spectral lines are relatively free from blending effects. We find that the higher speed yields a slightly better fit to the profiles of star A, while the lower speed is slightly better for star B, but both speeds are viable within the uncertainties of the data. Hence, we adopt v sin(i)=12.5 ±1 km s^{-1} as the most likely rotation speed of both stars. It

[6] http://www.as.utexas.edu/ chris/moog.html

[7] github.com/madamow/pymoogi

[8] pyastronomy.readthedocs.io/en/latest/pyasIDoc/asIDoc/rotBroad.html, github.com/sczesla/PyAstronomy/blob/master/src/pyasl/asl/rotBroad.py

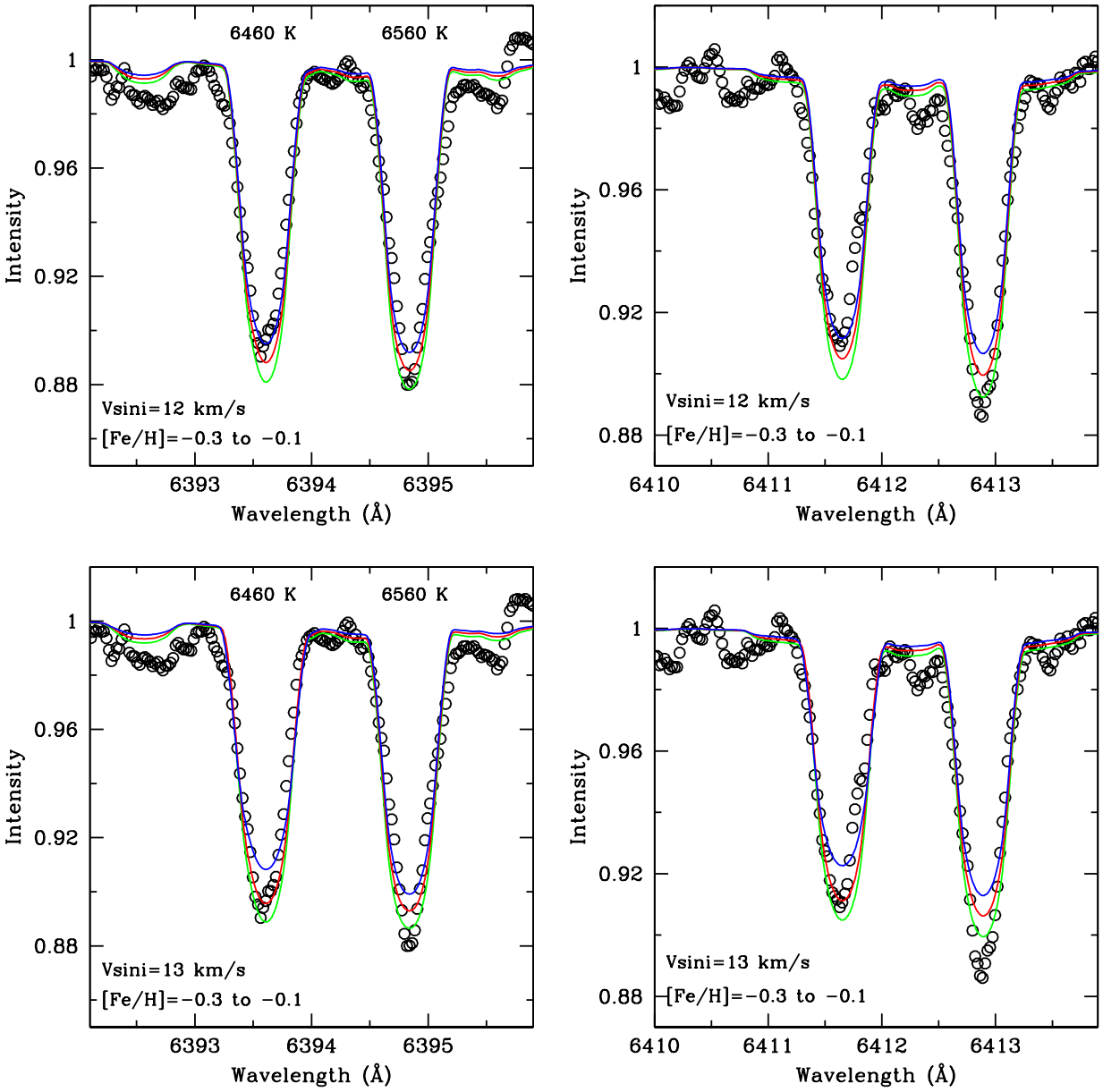

Figure 3. Determination of v sin(i): Shown are the rotationally-broadened synthetic line profiles from model atmospheres with T_{eff}, log(g), and ξ values from column 2 of Table 2, and for $[Fe/H] = -0.1$ (green), -0.2 (red) to -0.3 (blue). Rotational broadening v sin(i)=12 km s^{-1} (top) and 13 km s^{-1} (bottom) compare most favorable to the 5-point smoothed observations (dots).

is noteworthy that this value is smaller than the 15 km s^{-1} synchronous rotation velocity which was determined by T08, a discrepancy that we attribute to the lower spectral resolution of the T08 data compared to our echelle spectra.

For v sin(i) between 12 and 13 km s^{-1}, Figure 3 shows that the line profiles are consistent with $[Fe/H] = -0.10\pm0.05$ (star A) and -0.25 ± 0.1 (star B), similar to the result obtained from equivalent widths.

Figure 4 shows a selection of star A's lines compared to the synthetic line profiles from models with either T_{eff}=6460 K or 6600 K. The higher T_{eff} provides a better match to the observations and is particularly better for the Fe I λ6400 line because of the contribution from λ6400.316. This line contributes to the red wings of the blend. The lower temperature produces synthetic profiles with red wings that are clearly too extended.

The λ6400.316 line has an excitation potential 0.91 eV, compared to 3.60 eV for the λ6400.001 line, making it more sensitive to temperature. We conclude that, for star A, the best match to the line profile is with T_{eff}=6650$\pm$50 K, consistent with the $[Fe/H] = -0.15$ evolutionary track in Figure 2.

Given the constraint on the effective temperature ratio imposed by the light curve, the above results show that the

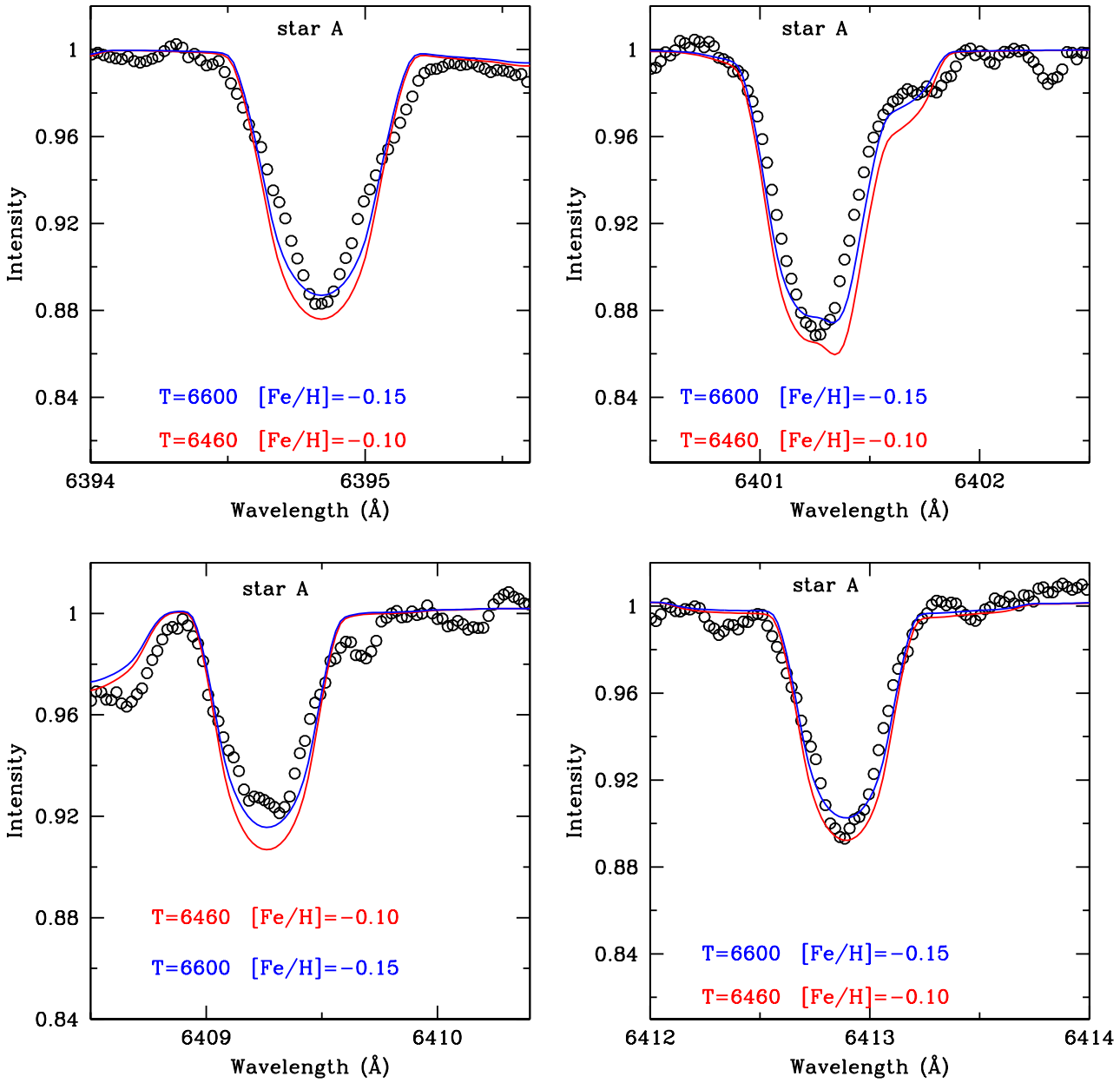

Figure 4. Line profiles of the primary star (dots) compared to model spectra with (T_{eff}, $[Fe/H]$)=(6460 K, −0.10) (red) and (T_{eff}, $[Fe/H]$)=(6600 K, −0.15) (blue). The model line profiles were broadened to v sin(i)=12 km s^{-1}. The λ6413 line is rather insensitive to T_{eff}, while λ6400.3 shows a relatively strong temperature sensitivity. This figure shows that models with $[Fe/H] > -0.1$ do not adequately represent the observations.

temperature of star A forced the effective temperature of star B to be 6550 K. Synthetic profiles computed with this temperature for star B are compared to the observations shown in Figure 5. We find that synthetic spectra with T_{eff} in the range 6460-6550 K yield viable fits to the observed profile. It is unclear whether this larger uncertainty in the secondary's temperature results from line profiles that are perturbed with respect to the predicted line shapes. What is clear is that $[Fe/H] > -0.1$ can be excluded for the entire temperature range. The constraints of the evolutionary tracks (Figure 2) lead to the conclusion that a higher temperature is favored.

5. Lithium abundance

The lithium abundance $A(Li)$ was constrained by comparing synthetic spectra constructed with MOOG with the observed spectrum in the $\lambda\lambda$6704–6710 wavelength range. We first analyzed $A(Li)$ by adopting effective temperatures of 6500 K and 6450 K, which approximately

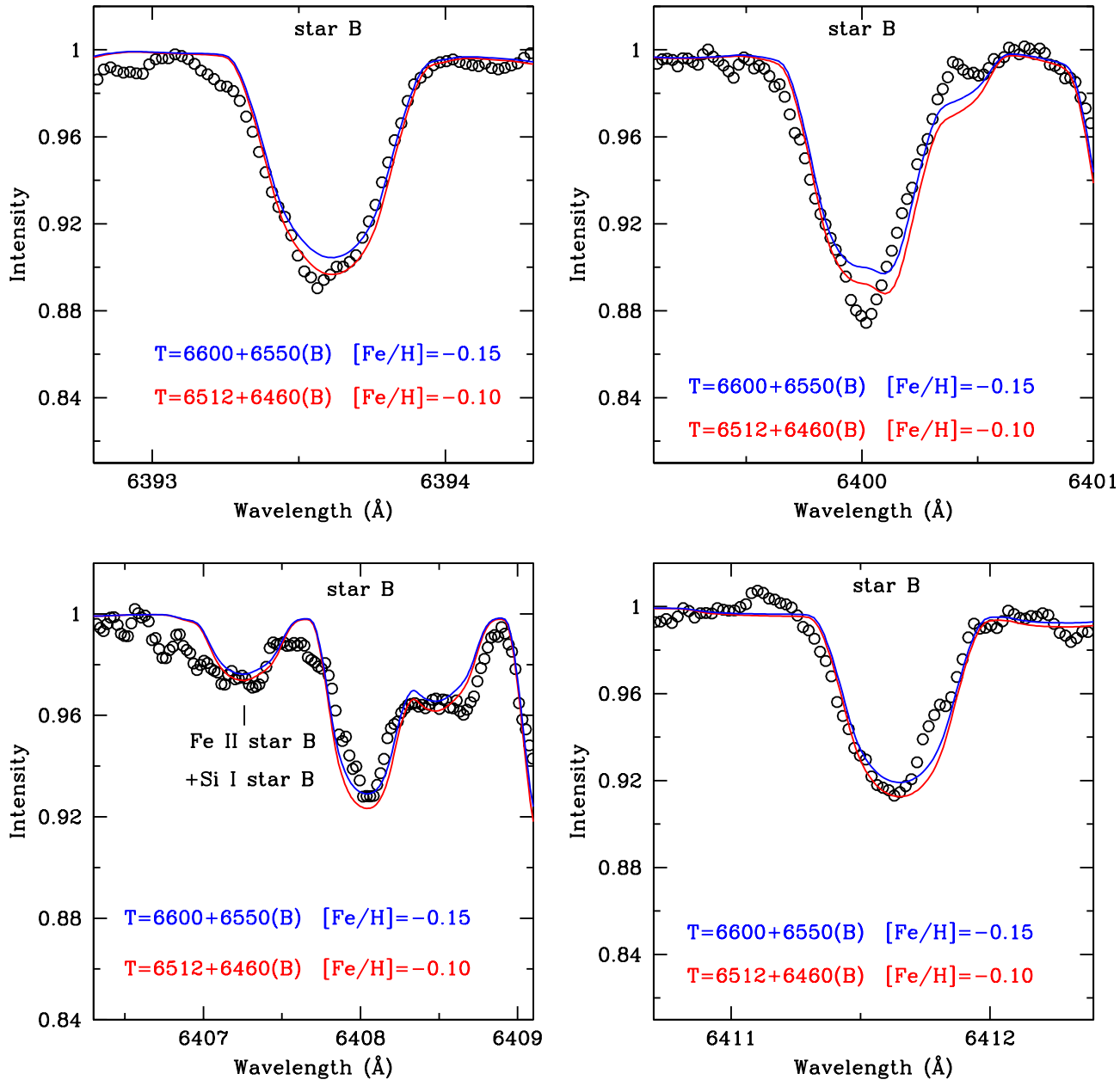

Figure 5. Line line profiles of the primary star (dots) compared to model spectra with (T_{eff}, $[Fe/H]$)=(6460 K, −0.10) (red) and (T_{eff}, $[Fe/H]$)=(6600 K, −0.15) (blue). The model line profiles are broadened to v sin(i)=12 km s^{-1}. The λ6413 line is rather insensitive to T_{eff}, while λ6400.3 shows a relatively strong temperature sensitivity. This figure shows that models with $[Fe/H] > -0.1$ would not adequately represent the observations.

correspond to those determined by T08. We found $A(Li)$ =2.45±0.07 (star A) and 2.25±0.1 (star B), values that are marginally consistent with those of Baugh et al. (2013) (2.67±0.1 and 2.42 ±0.2), and concluded that the two components seem to have slightly different Li abundances. A comparison between the synthetic spectra and observations for this case is shown in Fig. 6 (left panel).

We next analyzed the spectra under the assumption that the stars are hotter, 6650 K+ 6600 K, as implied by the λ6400 line profile. This yielded lithium abundances $A(Li)$=2.65±0.07 (star A) and 2.35±0.07 (star B), consistent with Baugh et al. (2013) determination. The strength of the Li lines does not have a significant dependence on the $[Fe/H]$ value; therefore, our results are not strongly dependent on the uncertainty in iron abundances. However, it depends more strongly on the effective temperature, as shown above. Our data are unfortunately too noisy to provide a constraint on the Li abundance to better than 0.05–0.1 dex, but both effective temperature sets do imply a somewhat lower $A(Li)$ in the secondary

Table 3. Results

Parameter	Literature	This paper		
		Equiv. Width	Line Prof.	Line Prof.
R_B/R_A	0.98	0.98f[a]	0.98f	0.98f
$[Fe/H]_A$	−0.15(.03)	−0.166(.07)[b]	−0.15(.05)	−0.15(.05)
$[Fe/H]_B$	−0.12(.03)	−0.239(.07)[b]	−0.15(.05)	−0.15(.05)
T_{Aeff}(K)	6512(50)	6512(adopted)	6500f	6600(50)
T_{Beff}(K)	6460(50)	6460(adopted)	6450f	6550(50)
v sin$(i)_A$ (km s^{-1})	⋯	⋯	12.5(.5)	12.5(.5)
v sin$(i)_B$ (km s^{-1})	⋯	⋯	12.5(.5)	12.5(.5)
$A(Li)_A$	2.67(.1)	⋯	2.45(.07)	2.65(0.07)
$A(Li)_B$	2.42(.2)	⋯	2.25(0.1)	2.35(.07)

[a]The "f" next to a value indicates that it was a fixed value.

[b]Values are the average of the results found from the two *IRAF/abfind* fits (solar microturbulent velocities 1 km s^{-1} and 0.8 km s^{-1}).

than in the primary. Future observations should aim for significantly higher S/N spectra to allow for more precise abundance determinations (as have been performed for the visual binary components of ζ Boo A and B by Strassmeier & Steffen (2022).

6. Discussion

In this study, we analyzed a high-resolution spectrum of the eclipsing binary V505 Per. The objective was to resolve three inconsistencies related to the chemical abundance of the two components: (a) The first is the subsolar Fe abundance reported by Baugh et al. (2013); Casagrande et al. (2011b), found from spectral and photometric analyses, which is inconsistent with the approximately solar abundance found by Southworth (2021) from the isochrone fitting. (b) The second is the Li abundance found by Baugh et al. (2013), which is factors of 2-5 larger than that observed in similar age and temperature single stars that lie in the Lithium Dip. (c) The third is the secondary Li abundance found by Baugh et al. (2013) is significantly lower than that of the primary, while both stars are expected to have the same age and therefore the same abundances. We first analyzed all available *TESS* photometric data to constrain the parameters that can be derived from the analysis of the eclipse light curve (Table 1), which, combined with the published solution for the radial velocity curves, yielded the first set of fundamental parameters for the system. Because the solution of the light curve only yields the sum of the stellar radii ($R_A + R_B$) and not the ratio, we used theoretical evolutionary tracks to constrain the value of R_B/R_A. We found that for a fixed value $R_A + R_B$ as derived from the light curve, neither the R_B/R_A nor the temperature ratio T_A/T_B strongly depends on metallicity, with the solar and subsolar options yielding nearly identical values. However, the actual temperature strongly depends on metallicity. If the previously published temperatures (T08) are adopted, then the system's metallicity is at least solar, as concluded by S21, but the system is significantly older (1.5 Gyr instead of ∼1 Gyr). However, if instead the values of $[Fe/H]$ are as low as determined by Baugh et al. (2013) and Casagrande et al. (2011b), then T_{eff} must be approximately T_{Aeff} ∼6670 K and T_{Beff} ∼6620 K. We compared our observed spectrum with stellar atmosphere models with T_{eff}/K in the range [6400, 6800] and $[Fe/H]$ in the range [-0.4, -0.1] and found that $[Fe/H]$ values larger than −0.1 could be excluded. Specifically, for the primary/secondary star we found $[Fe/H]$=−0.17±0.07/−0.25±0.07 from Fe I equivalent widths (§ 4.1). By comparing synthetic and observed line profiles, we found $[Fe/H] \sim -0.13\pm0.05$ (Figures 4 and 5). Most of the primary star's line profiles are best reproduced with T_{eff} ∼6600 K and $[Fe/H] = -0.15$ (Figure 4). From the temperature ratio, which is fixed by the light curve solution, this implies that the secondary's effective temperature is ∼6550 K. However, we find that synthetic spectra with T_{eff} in the range 6460-6550 K yield viable fits to the observed profile. It is not clear whether the larger uncertainty in the secondary derived parameters results from line profiles that seem somewhat perturbed with respect to the predicted line shapes. Having found that temperatures higher than the T08 values are viable, we proceeded to fit synthetic lithium line profiles to the observations. The only well-resolved Li I lines in our spectrum are those of the λ6707.83 blend. The strength of these lines is significantly more dependent on T_{eff} than on $[Fe/H]$. Thus, we modeled the Li lines with the T08 temperatures (for consistency with the results of Baugh et al., 2013) as well as at temperatures 150 K higher. We found $A(Li)$ values that are consistent with those determined by Baugh et al. (2013) within their uncertainties, and we also confirmed that the lithium abundance of the secondary was slightly lower than that of the primary.

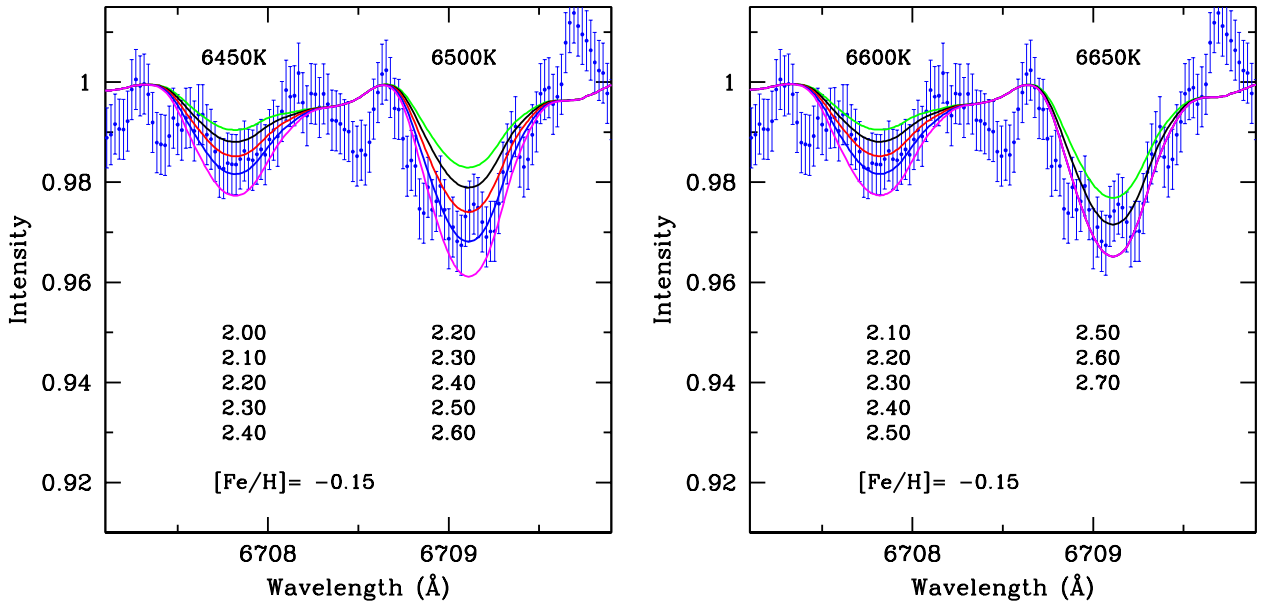

Figure 6. Synthetic spectra with different lithium abundances compared to the observed 5-point smoothed data (dots). The model A(Li) values for each star are listed below the corresponding Li line. The top value (green) corresponds to the curve with the smallest A(Li), and the bottom corresponds to the largest. The error bars indicate a 0.6% uncertainty in the 5-point smoothed data. **Left:** Composite model spectra with T08 effective temperature. **Right:** T_{eff} =(6650 K, 6600 K) for stars A and B, respectively. The synthetic spectra are all broadened to v sin(i)=12 km s^{-1}.

6.1. Higher temperatures eliminate the discrepancy with the Lithium Dip

A higher T_{eff} places the stars at the hot limit of the Lithium dip where there is a steep rise in $A(Li)$, eliminating the discrepancy between their $A(Li)$ and that of cluster stars of a similar age. This is illustrated in Figure 7, where we plot $A(Li)$ *vs.* T_{eff} from Balachandran (1995) for the Hyades cluster (age ∼ 625 Myr), Praesepe (age ∼680 Myrs), and and NGC752 (age estimates ranging from 1.34 to 1.61 Gyr).

Higher temperatures are also more in line with the Mass-T_{eff} relation for NGC 752 than with that of the younger clusters, as shown in Figure 8, where we plot the same stars as in Figure 7 with data from Balachandran (1995).

Lithium is destroyed by proton capture in stellar interiors at a temperature ∼2.5 million degrees. In main sequence solar-type stars (M∼1.0±0.10 M$_\odot$), this temperature is reached below the base of the surface convective zone, which makes it unlikely for Li-depleted material to reach the surface unless there is an additional mechanism that transports it to the convective zone. In the absence of such a mechanism, the surface Li abundance during the main sequence is not predicted to be anomalous. However, evidence for the existence of such an additional mechanism is clearly found, for example, in plots of $A(Li)$ *versus* effective temperature T$_{eff}$ in main sequence cluster stars with 6300< T_{eff} <6900 K (Boesgaard & Tripicco, 1986; Boesgaard & King, 2002) in what is called the *Li Dip*. The mechanism responsible for excess mixing during the main sequence is thought to be associated with stellar rotation. In binaries, it has long been suspected that the presence of a companion can impact the manner in which the mixing process proceeds. This is particularly true for tidally locked systems, in which differential rotation and strong currents should be suppressed, thus inhibiting strong mixing. However, asynchronous binaries may provide a mechanism by which enhanced mixing can occur as a consequence of local differential rotation gradients (Song et al., 2013; Koenigsberger et al., 2021).

Our results indicate that both components of V505 Per rotate subsynchronously. However, this result was based on a single orbital phase near conjunction. The *TESS* light curve displays a clear ellipsoidal effect, implying that the stars are distorted from a purely spherical shape. Thus, observations at other orbital phases are required to determine whether the stars are truly in subsynchronous rotation or if they undergo line profile variability, which makes the line profiles appear narrower near conjunction.

6.2. Higher temperatures are still consistent with the SED

A higher effective temperature has an impact on the spectral energy distribution (SED), so the natural question that arises is whether the SED of a T_{eff}=6650 K + 6550 K system is consistent with the observations. [9]

[9]There can be differences of up to 200 K in the effective temperatures as determined photometrically, depending on the calibrations that are used, which has an impact on the $[Fe/H]$ values; see, for example, Balachandran

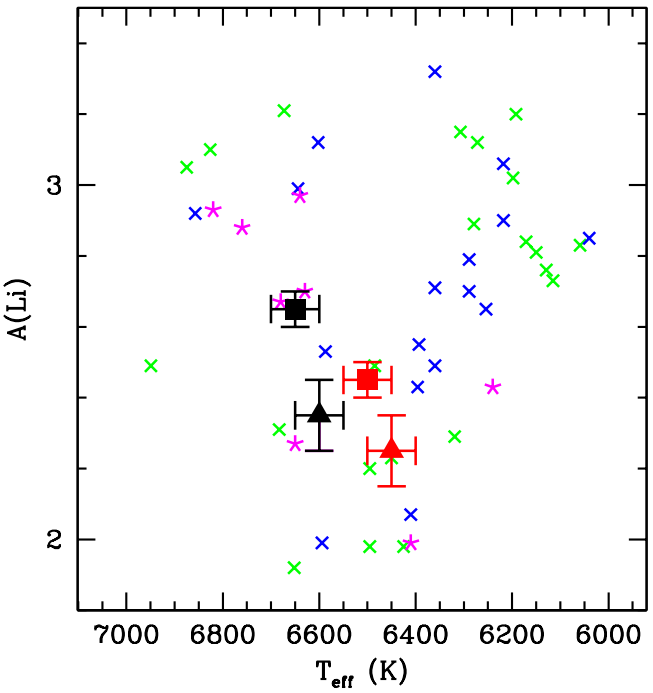

Figure 7. Lithium abundance as a function of effective temperature. Crosses indicate data from Balachandran (1995) as follows: Hyades (green, age ∼ 625 Myr), Praesepe (blue, age ∼680 Myrs), and NGC752 (magenta, age estimates ranging from 1.34 to 1.61 Gyr). Our determinations are shown with a filled-in square for star A and a filled-in triangle for star B. Red/black symbols correspond to the lower/higher effective temperatures (Table 3).

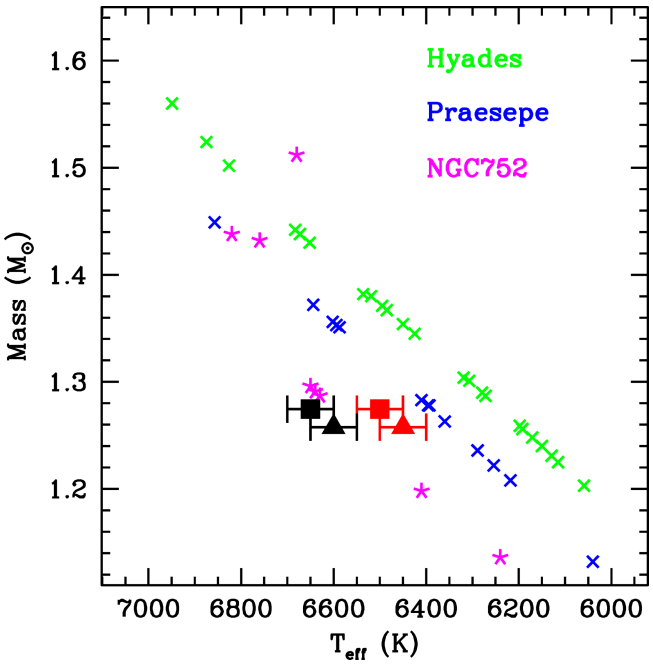

Figure 8. The Mass-Effective Temperature data from Balachandran (1995) (open squares) for the same stars plotted in Figure 7. The filled-in square and triangle are as follows: Hyades (green, age ∼ 625 Myr), Praesepe (blue, age ∼680 Myrs), and NGC752 (red, age estimates ranging from 1.34 to 1.61 Gyr). Our star A determinations are shown with a filled-in squares and starB with filled-in triangles.

We now show that higher T_{eff} values are consistent with the observed SED. In Figure 9 we plot the observed absolute flux in different wavelength bands available in the literature. Specifically, we used the Bp, G, and Rp fluxes, absolute flux calibrated as given in Vizier (Ochsenbein et al., 2000), referring to the GAIA DR3 data release (Riello et al., 2021), to the 2MASS sky survey (Skrutskie et al., 2006) for the Johnson filter J, H, K measurements (nominal effective wavelengths 1250 nm, 1630 nm, and 2190 nm respectively), and the Gaia XP spectrum (De Angeli et al., 2023). The latter is approximately 5 % brighter than the other Gaia fluxes; therefore, we scaled the XP spectrum by 0.95 to bring it into agreement with the other Gaia fluxes. The absolute fluxes are compared to composite model SEDs for three effective temperatures assuming stellar radii as determined by S21 (1.294 $R_\odot$ and 1.264 $R_\odot$) and a distance $D = 62.14 \pm 0.12$ pc, which results from a Gaia DR3 parallax of $\pi = 16.068 \pm 0.02$ mas and a zero point correction of $Z5 = -0.024$ mas according to the recipe given by (Lindegren et al., 2021).[10]

The models were interpolated for log(g)=4.3, $[M/H]$=−0.25 and T_{eff}= 6500 K, 6625 K, and 6750 K from the Atlas9 Castelli-Kurucz grids (Castelli & Kurucz, 2003)[11].

For each of the effective temperatures, the SEDs are reddened, respectively, by $E(B-V) = 0, = 0.02$, and $= 0.03$ It can be seen that there is no significant difference between these models and the observed energy distribution.

However, the obvious difference between the models and the absolute fluxes is that the models have about a 3 % too small flux in the infrared. The dominant uncertainty at these wavelengths are the Johnson filter measurements, which for the K filter is ±2 %. Thus, the difference is statistically not significant but it seems to be real because it is for both the H and K filters at approximately the same ratio. Any absolute difference at optical wavelengths can be compensated for by reddening.

7. Conclusions

Adopting the T_{eff} values from T08, Baugh et al. (2013) determined lithium abundances that are significantly higher than the lithium abundance in similar-age cluster stars at the same temperature. They also found that star A and star B have marginally different $A(Li)$. We repeated this

(1995). NOTE: This author (and others?) plot A(Li) vs. τ_{ZAM}. This means that for the older clusters, they have to assume an evolutionary model predicting the T_{ZAMS} given the current T_{eff} and the age of the system.

[10] S21 determined a distance D=61.19±0.62 pc to the system, while the *Gaia* (re-interpreted) EDR3 parallaxes give 62.03±0.10 pc (Bailer-Jones et al. (2021)).

[11] https://wwwuser.oats.inaf.it/fiorella.castelli/grids/gridp00k2odfnew/fp00k2tab.html

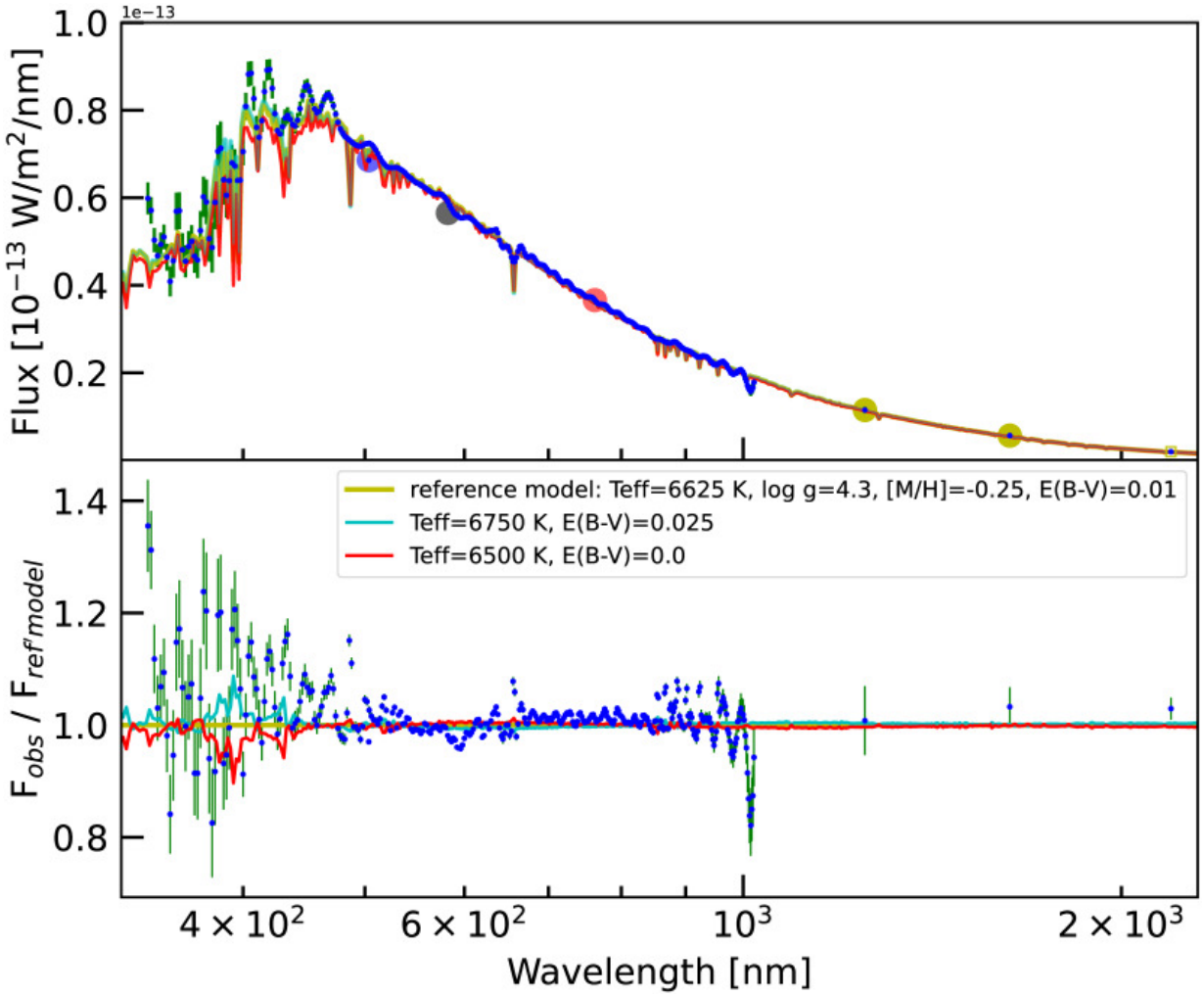

Figure 9. Top: Observed spectral energy distribution of V505 Per compared to theoretical SEDs for two stars with T_{eff}= 6500 K (red), 6625 K (dark green, Reference Model), and 6750 K (light green), and adopting a distance $D = 62.14 kpc$. The observations are as follows: large blue, grey, and red circles for the Gaia Bp, G, and Rp fluxes, respectively. large yellow circles and small blue point for Johnson J, H, and K fluxes; small blue points with green error bars for the Gaia spectral energy distribution (scaled by a factor 0.95 to make it consistent with the Gaia Rp filter flux, see text). Bottom: Ratios of the observed SED models with the reference model in the denominator. Narrow peaks in the ratio result from a mismatch of resolution, because the Kurucz model has a higher resolution than the Gaia XP low resolution data. This mismatch is particularly prominent in the hydrogen line wavelengths. Also shown are the ratios of T_{eff} =6500 K and 6750 K models to the reference model. Differences between these models and the reference model are only visible in the 400 nm region where the hotter model has a ratio larger than unity, and the cooler less than unity. In this wavelength region the combination of several strong narrow absorption lines in the Kurucz reference model and relatively large uncertainties in the observations makes it difficult to judge which model provides the best fit, although it seems likely that that the reference model with T_{eff} =6625 provides the best fit. Thus, we conclude that the observed SED is consistent with hotter T_{eff} than those determined by T08.

analysis with our R=100,000, S/N∼100 echelle spectrum to confirm these results. However, our analysis of the Fe I line profiles suggests that T_{eff} could be at least 150 K larger than the values determined by T08. Allowing for hotter T_{eff}, we find that both stars lie near the hot edge of the Lithium Dip, where such abundances are not uncommon. Higher T_{eff} values also help relieve the tension between the model line profiles of the λ6400.35 absorption line, because at lower temperatures, the red wing of the line profile is significantly stronger than that observed. In addition, the combined constraints of the eclipse light curve and the evolutionary tracks require higher T_{eff} values to satisfy the results obtained by us and other authors that $[Fe/H]$ is subsolar. The higher effective temperatures suggested by our analysis would still be consistent with the observed spectral energy distribution of the V505 Per system, although marginally larger K-band fluxes are observed than predicted by the models. If this difference is real, V505 Per may contain an as yet undetected, low mass third object.

Further high S/N and spectral resolution observations are needed to allow for more precise abundance determinations, as well as to check for orbital phase-dependent variations that could affect the line strengths and profiles, particularly because we find the stars to be in subsynchronous rotation and hence could be undergoing tidally driven perturbations which are dependent on the orbital phase.

Support from the UNAM DGAPA PAPIIT program IN105723 and the Indiana University Institute for Advanced Study are gratefully acknowledged. GK and AM thank Andrew Tkachenko for his useful comments during the early phase of this investigation.

References

Adamow, M. M. 2017, in AAS, Vol. 230, 216.07
Bailer-Jones, C. A. L., Rybizki, J., Fouesneau, M., Demleitner, M., & Andrae, R. 2021, AJ, 161, 147, doi: 10.3847/1538-3881/abd806
Balachandran, S. 1995, ApJ, 446, 203, doi: 10.1086/175779
Baugh, P., King, J. R., Deliyannis, C. P., & Boesgaard, A. M. 2013, PASP, 125, 753, doi: 10.1086/671721
Boesgaard, A. M., & King, J. R. 2002, ApJ, 565, 587, doi: 10.1086/324436
Boesgaard, A. M., & Tripicco, M. J. 1986, ApJ, 303, 724, doi: 10.1086/164120
Casagrande, L., Schöenrich, R., Asplund, M., et al. 2011a, VizieR Online Data Catalog: Geneva-Copenhagen survey re-analysis (Casagrande+, 2011), VizieR On-line Data Catalog: J/A+A/530/A138. Originally published in: 2011A&A...530A.138C, doi: 10.26093/cds/vizier.35300138
Casagrande, L., Schönrich, R., Asplund, M., et al. 2011b, A&A, 530, A138, doi: 10.1051/0004-6361/201016276
Castelli, F., & Kurucz, R. L. 2003, in IAUS, Vol. 210, Modelling of Stellar Atmospheres, A20, doi: 10.48550/arXiv.astro-ph/0405087
De Angeli, F., Weiler, M., Montegriffo, P., et al. 2023, A&A, 674, A2, doi: 10.1051/0004-6361/202243680
del Burgo, C., & Allende Prieto, C. 2018, MNRAS, 479, 1953, doi: 10.1093/mnras/sty1371
do Nascimento, J. D., J., Charbonnel, C., Lèbre, A., de Laverny, P., & De Medeiros, J. R. 2000, A&A, 357, 931, doi: 10.48550/arXiv.astro-ph/0003010
Ginsburg, A., Sipőcz, B. M., Brasseur, C. E., et al. 2019, AJ, 157, 98, doi: 10.3847/1538-3881/aafc33
Gustafsson, B., Edvardsson, B., Eriksson, K., et al. 2008, A&A, 486, 951, doi: 10.1051/0004-6361:200809724
Holmberg, J., Nordström, B., & Andersen, J. 2007, A&A, 475, 519, doi: 10.1051/0004-6361:20077221
Koenigsberger, G., Moreno, E., & Langer, N. 2021, A&A, 653, A127, doi: 10.1051/0004-6361/202039369
Kurucz, R. L. 1992, in IAUS, Vol. 149, The Stellar Populations of Galaxies, ed. B. Barbuy & A. Renzini (Kluwer Academic Publishers, Dordrecht), 225
Kwee, K. K., & van Woerden, H. 1956, BAN, 12, 327
Lightkurve Collaboration, Cardoso, J. V. d. M., Hedges, C., et al. 2018, Lightkurve: Kepler and TESS time series analysis in Python, Astrophysics Source Code Library, record ascl:1812.013
Lindegren, L., Bastian, U., Biermann, M., et al. 2021, A&A, 649, A4, doi: 10.1051/0004-6361/202039653
Mowlavi, N., Eggenberger, P., Meynet, G., et al. 2012, A&A, 541, A41, doi: 10.1051/0004-6361/201117749
Ochsenbein, F., Bauer, P., & Marcout, J. 2000, A&AS, 143, 23, doi: 10.1051/aas:2000169
Pavlovski, K., Southworth, J., Tkachenko, A., Van Reeth, T., & Tamajo, E. 2023, A&A, 671, A139, doi: 10.1051/0004-6361/202244980
Pourbaix, D., Tokovinin, A. A., Batten, A. H., et al. 2004, A&A, 424, 727, doi: 10.1051/0004-6361:20041213
Prša, A., Harmanec, P., Torres, G., et al. 2016, AJ, 152, 41, doi: 10.3847/0004-6256/152/2/41
Prša, A., Kochoska, A., Conroy, K. E., et al. 2022, ApJS, 258, 16, doi: 10.3847/1538-4365/ac324a
Ricker, G. R., Winn, J. N., Vanderspek, R., et al. 2015, JATIS, 1, 014003, doi: 10.1117/1.JATIS.1.1.014003
Riello, M., De Angeli, F., Evans, D. W., et al. 2021, A&A, 649, A3, doi: 10.1051/0004-6361/202039587
Skrutskie, M. F., Cutri, R. M., Stiening, R., et al. 2006, AJ, 131, 1163, doi: 10.1086/498708
Sneden, C., Bean, J., Ivans, I., Lucatello, S., & Sobeck, J. 2012, MOOG: LTE line analysis and spectrum synthesis, Astrophysics Source Code Library, record ascl:1202.009
Song, H. F., Maeder, A., Meynet, G., et al. 2013, A&A, 556, A100, doi: 10.1051/0004-6361/201321870
Southworth, J. 2021, Obs, 141, 234, doi: 10.48550/arXiv.2106.04323
Strassmeier, K. G., & Steffen, M. 2022, AN, 343, e20220036, doi: 10.1002/asna.20220036
Swade, D., Fleming, S., Mullally, S., et al. 2019, in ASPC, Vol. 523, Astronomical Data Analysis Software and Systems XXVII, ed. P. J. Teuben, M. W. Pound, B. A. Thomas, & E. M. Warner, 453
Thorburn, J. A., Hobbs, L. M., Deliyannis, C. P., & Pinsonneault, M. H. 1993, ApJ, 415, 150, doi: 10.1086/173152
Tomasella, L., Munari, U., Siviero, A., et al. 2008, A&A, 480, 465, doi: 10.1051/0004-6361:20078384
Wallace, L., Hinkle, K., & Livingston, W. 1998, An atlas of the spectrum of the solar photosphere from 13,500 to 28,000 cm-1 (3570 to 7405 A)